Bandwidth-Enhanced Circularly Polarized mm-Wave Antenna With On-Chip Ground Plane

Benedikt Sievert, *Member, IEEE*, Jonathan Wittemeier, Jan Taro Svejda, *Member, IEEE*, Nils Pohl, *Senior Member, IEEE*, Daniel Erni, *Member, IEEE*, and Andreas Rennings, *Member, IEEE*

***Abstract*— This article presents a design methodology and a realization of an antenna radiating circular polarization (CP) for Frequency Modulated Continuous Wave (FMCW) radar at mm-wave frequencies on-chip, which combines antennas of different resonance frequencies to increase the operation bandwidth and allow for high-resolution radar. The antenna consists of four dipoles with an on-chip ground plane operating at two resonance frequencies combined with a matching and feeding network, which enables both frequency selectivity in advantage for the resonant antenna and radiation of circular polarization. The dipole arms are based on shorted λ/4 resonators, which are enhanced with series capacitances for increased radiation efficiency. A method for the broadband characterization of CP antennas and the measurement results of the designed CP antenna are presented. It is shown that the antenna covers a bandwidth between 220 and 260 GHz, indicating the feasibility of both the measurement method and the antenna concept.**

***Index Terms*— Antenna measurements, circular polarization, millimeter-wave technology, SiGe/Si technologies, system on-chip.**

I. Introduction

ONE key motivation of utilizing mm-waves up to sub-THz for radar, material characterization, and communication is the increased absolute bandwidth, even for narrowband systems, compared with their lower frequency counterparts, and the small antennas with reasonable apertures [1]–[4]. Furthermore, with increasing frequency, the decreasing single antenna size allows for the integration of the antenna on-chip [5], reducing interconnection losses and increasing the degrees of freedom in antenna design compared with an antenna in package [6]. This article presents an on-chip antenna with an on-chip ground plane and a sophisticated combined antenna and feeding structure to radiate a broadband elliptical polarization to approximate a circular polarization (CP). Antennas with an on-chip ground plane are usually resonant and thus inherently band-limited, which also relates to the bandwidth of the generated CP [7]. Although backside-radiating chip antennas with high-permittivity lenses can easily achieve a wider bandwidth and higher efficiency [8], [9], the use of on-chip ground planes for frontside-radiating antennas eases the packaging process, since neither flip-chip bonding nor lens positioning is necessary [10]. Alternatively, the use of off-chip ground planes [11] or thick substrates [12], [13] usually allows for a wideband CP operation. However, for higher frequencies, substrate waves in the thick substrate [5] need to be suppressed or to become insignificant due to the use of a high-gain lens. Furthermore, the high gain associated with the utilized lens finally limits the applicability in large antenna arrays in combination with beam-steering [14], since the principle of pattern multiplication ultimately reduces the array performance off broadside. With the utilized CP, each reflection will change the polarization from left-handed (LH-) to right-handed CP (RHCP) and vice versa. Thus, the detection of simple targets demands different polarized Tx and Rx antennas or a quadrature hybrid coupler, which feeds two orthogonal polarizations, as in [8]. The antenna introduced here utilizes capacitive discontinuities in quarter-wavelength grounded dipole arms to increase the radiation efficiency [15], [16]. Furthermore, the full antenna design process is presented, and characterization of the antenna's polarization up to 280 GHz is carried out utilizing a rotating rectangular waveguide and maintaining a phase-correct antenna measurement.

This article is organized as follows. Section II will present a generic antenna design to maximize the utilization of the available chip area. Furthermore, the differential feeding network concept assuring frequency selectivity and correct feeding phases for the CP generation is introduced. Based on the single component, Section III shows the total antenna assembly and simulated current density for physical insight. To measure the radiated polarization, Section IV describes the utilized measurement method for polarization-switchable phase-stable mm-wave measurements at each far-field sampling point. Finally, Section V presents the measured characteristics of the antenna fabricated in the Infineons B11HFC silicon–germanium technology and compares these with full-wave simulation results.

II. Design Methodology

The overall CP antenna presented here consists of eight circularly arranged antenna elements fed with a

Manuscript received 22 December 2021; revised 6 May 2022; accepted 30 May 2022. Date of publication 24 June 2022; date of current version 9 November 2022. This work was supported by the German Research Foundation ("Deutsche Forschungsgemeinschaft") (DFG) under Project 287022738 TRR 196 MARIE for Projects C03, C05. *(Corresponding author: Benedikt Sievert.)*

Benedikt Sievert, Jan Taro Svejda, Daniel Erni, and Andreas Rennings are with the Laboratory for General and Theoretical Electrical Engineering (ATE), Center for Nanointegration Duisburg-Essen (CENIDE), University of Duisburg-Essen, D-47048 Duisburg, Germany (e-mail: benedikt.sievert@uni-due.de).

Jonathan Wittemeier and Nils Pohl are with the Institute of Integrated Systems, Ruhr University Bochum, D-44801 Bochum, Germany.

Color versions of one or more figures in this article are available at https://doi.org/10.1109/TAP.2022.3184539.

Digital Object Identifier 10.1109/TAP.2022.3184539

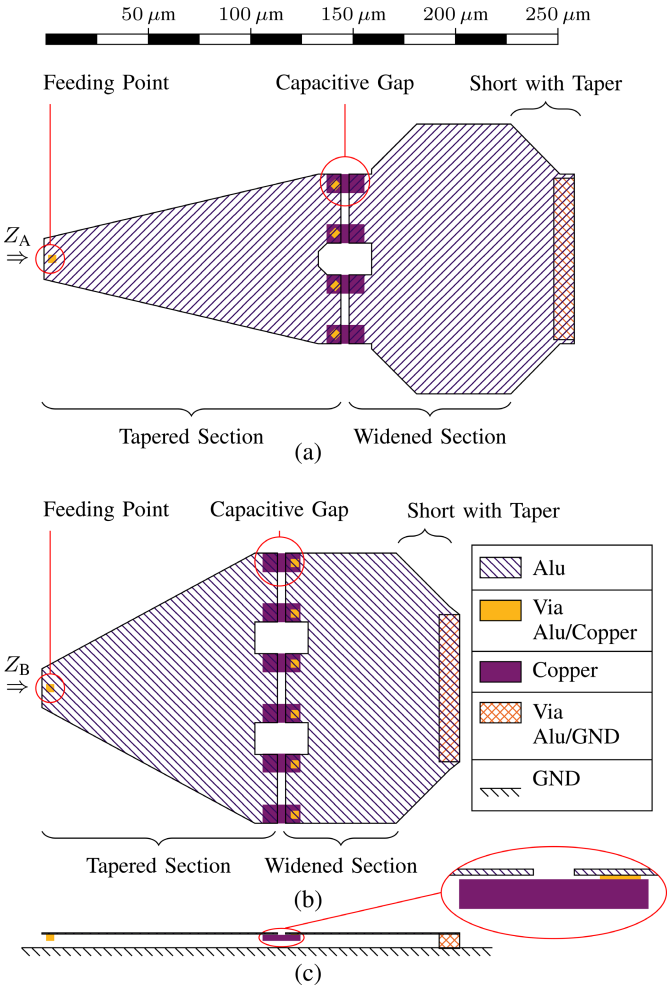

Fig. 1. (a) and (b) Top view on the dipole arms A and B including the feeding point, a tapered section toward the capacitive gap, and a widened section carrying the largest current densities toward the short. Both ground and substrate are not shown for reasons of clarity. (c) Cross section of (b) with an enlarged capacitive gap.

frequency-selective feeding network, where the antenna elements utilize most of the available chip area by design (see Fig. 7). In detail, each antenna element is a shorted $\lambda/4$ resonator, such that a pair of two opposing elements build a $\lambda/2$ dipole with shorted ends. Each of these elements will be referred to as dipole arms to emphasize their final function. Here, the central feeding eases the feeding network design, as will be discussed later (see Section II-B). Since both conductor and dielectric losses usually allow for only moderate radiation efficiencies, special attention is paid to increasing the radiation efficiency by inserting a capacitive discontinuity [15], [16].

A. Antenna Element Design

Fig. 1(a) and (b) shows the single antenna element geometry for both utilized elements. Within this publication, these elements will be referred to as A and B. Although omitted in most of the drawings presented here for reasons of clarity, the whole antenna is located over a ground plane on the lowermost on-chip layer with ≈ 9 μm distance and surrounded by SiO_2.

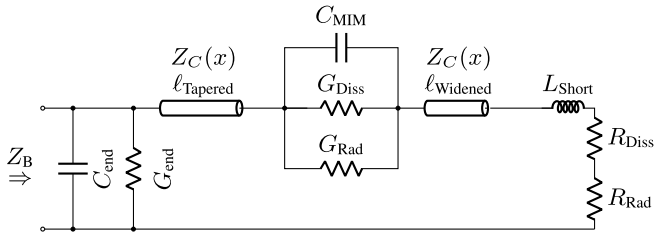

Fig. 2. EC model for antennas A and B. The corresponding EC elements are given in Table I.

The rather unusual shape of the antennas allows for a densely packed arrangement on-chip to fully utilize the available chip area, as will be shown in Section III. The short at the end of the antenna allows for a much shorter realization of a $\lambda/4$ dipole arm [17, p. 7-3] at the expense of higher losses compared with a $\lambda/2$ resonator with an open termination. Especially due to the multilayered via structures used to realize the short and the close proximity of the ground plane, large dissipative conductor losses are expected. To overcome this drawback, a radiating capacitive discontinuity is introduced into the antenna increasing the radiation efficiency to a suitable level. A thorough discussion on the effects of the discontinuity on the bandwidth and efficiency is presented in [15]. Additionally, a full explanation of the radiation mechanism can be found in [18] and [19].

Based on the equivalent circuit (EC) from [16], an EC model for the dipole arms is depicted in Fig. 2. Since both dipole arms A and B share the same principle of operation, their general EC is identical, and only the EC elements differ due to the different antenna geometries. Starting from the antenna's feeding point at the open end, which is modeled by a capacitance C_{End} and a radiation conductance G_{End} according to [18] and [20], a tapered microstrip section is followed by a capacitive discontinuity. After the discontinuity, a widened microstrip section is terminated by a short circuit to ground. At resonance, the high impedance at the feeding point will result in low current and thus comparably smaller losses in the narrow part of the tapered section. Along the antenna length, the current increases toward the short, only affected by the discontinuity as discussed in [16]. The discontinuities are controlled by the overlap of the top aluminum and the underlying copper layer [see Fig. 1(c)], and are described by the capacitance C_{MIM}, a dissipation conductance G_{Diss} accounting for ohmic and dielectric losses, and a radiation conductance G_{Rad} to model the radiation of the gap. They yield both an increased radiation efficiency and a further degree of freedom in the antenna design, where the antenna length can be partly compensated by the capacitance, enabling frequency-tuning without modifying the antenna length. The short circuit is described by the series inductance L_{Short}, the dissipation resistance R_{Diss} accounting for mainly ohmic losses, and the radiation resistance R_{Rad}. Here, the radiation resistance of a dipole in a grounded dielectric according to [21, p. 42] can be used for R_{Rad}, and the microstrip line is well described by characteristic impedance [22] and conductor losses [23] by the incremental inductance rule. All remaining EC elements are

TABLE I

EC ELEMENTS AT 230 AND 250 GHz FOR ANTENNAS A AND B, RESPECTIVELY (SEE FIG. 2)

Ant.	$Z_{C,\,min}$	$Z_{C,\,max}$	L_{Short}	R_{Diss}	R_{Rad}
A	11.5 Ω	46.9 Ω	0.313 pH	63.0 mΩ	4.44 mΩ
B	11.5 Ω	48.3 Ω	0.254 pH	37.2 mΩ	5.01 mΩ
Ant.	C_{end}	G_{end}	C_{MIM}	G_{Diss}	G_{Rad}
A	0.720 fF	17.2 μS	38.4 fF	10.3 μS	0.638 mS
B	0.722 fF	20.4 μS	69.6 fF	42.8 μS	2.65 mS

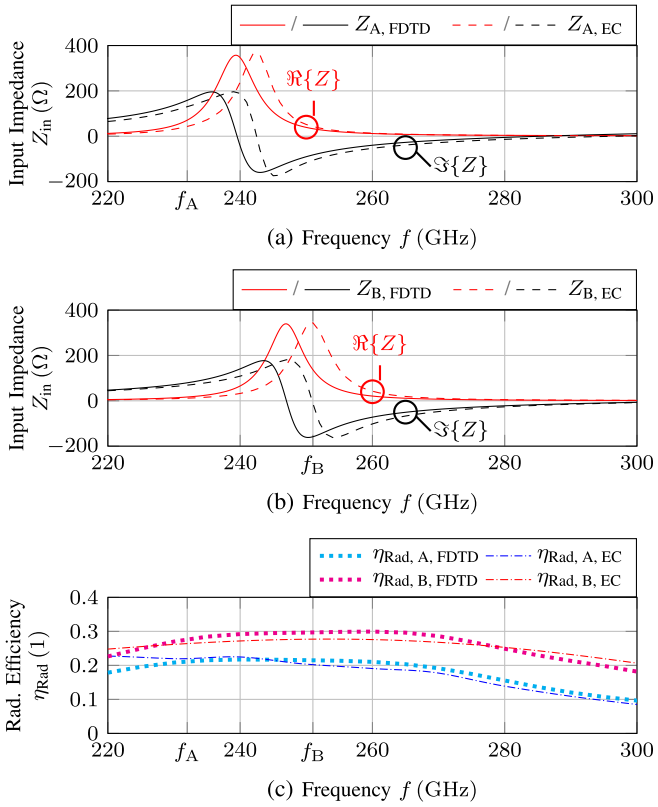

Fig. 3. (a) and (b) Simulated input impedance of the dipole arms A and B and (c) corresponding radiation efficiency without mismatch losses. Markers f_A and f_B highlight the intended operating frequency. Both input impedances show the behavior of a shorted $\lambda/4$ resonator, and their respective matching at f_A and f_B will be accomplished by the feeding network depicted in Fig. 5.

extracted as general functions of frequency between 220 and 300 GHz according to the method from [16]. Table I gives the EC elements evaluated at the operation frequencies of the respective antennas. Both antenna elements A and B are designed not only to geometrically match each other and the available chip area but also to operate at different frequencies f_A and f_B in combination with the feeding and matching network. Fig. 3(a) and (b) depicts the input impedance for both antennas, which indicates the $\lambda/4$ resonances, calculated by an FDTD solver and with a circuit simulation of the presented ECs. Given the simplicity of the ECs, the agreement to the full-wave simulation is very good, where only a small frequency shift can be observed. Here, it should be emphasized that the dipole arms A and B will be detuned by the matching network to obtain the operation at f_A and f_B. Furthermore, Fig. 3(c) shows the simulated radiation efficiency for both antenna elements, intended to operate at $f_A = 230$ GHz and

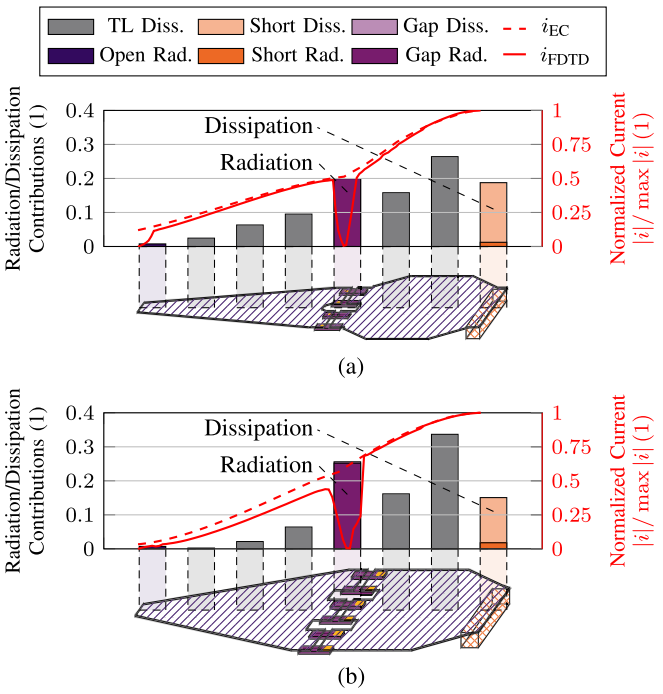

Fig. 4. Evaluation of the power contributions to radiation and dissipation and the normalized antenna current for (a) antenna A at 230 GHz and (b) antenna B at 250 GHz.

$f_B = 250$ GHz for A and B, respectively. Here, the agreement between FDTD result and EC modeling is very good.

Finally, the EC description enables physical insight into the radiation mechanism of the antenna, as depicted in Fig. 4. Here, the contributions to radiation and dissipation losses are visualized for different parts of the dipole arms at their respective operation frequencies. These antenna parts are the open-ended feeding point, TL sections of each $\approx$ 50 μm length, the capacitive gap, and the short circuit at the via. The power contributions are separated into dissipation and radiation for each element to allow for interpretation of its use in the overall antenna. The main radiation contributions result from the capacitive gap and the short circuit, and only a very small fraction is radiated by the open circuit. The losses are mainly caused by the via and the wide TL sections, which is reasoned by the current distribution depicted as well. Since both arms are operated close to their $\lambda/4$ resonance, the current peaks at the antenna end, resulting in the largest loss contributions. For comparison, both the current distributions calculated by the circuit simulation and the FDTD method are given, showing a very good agreement as well. The minimum current calculated by the FDTD at the capacitive gap results from the current being calculated only on the uppermost aluminum layer, neglecting currents in the MIM layers. The input impedance and the corresponding matching conditions will be highlighted in the next paragraph.

B. Feeding Network Design

Within the operation bandwidth of the antenna elements, the feeding network should enable a good matching condition for each four of the eight elements by its frequency selectivity

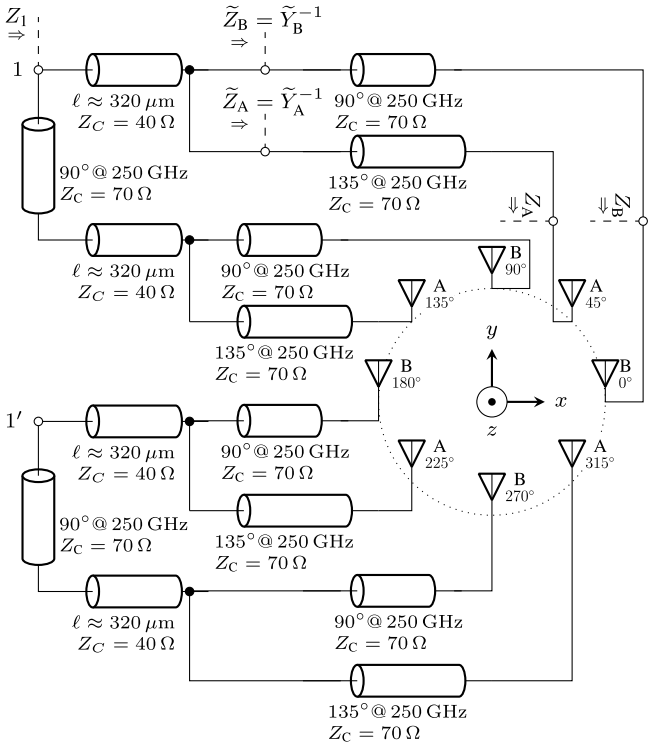

Fig. 5. Schematic of the feeding and matching network including each four antennas A and B, their respective input impedances Z_A and Z_B, their impedance after transformation $\widetilde{Z}_A$ and $\widetilde{Z}_B$, and the total input impedance Z_1 corresponding to a differential feeding at 1 and 1′. The lengths and impedances (Z_C) of the TLs are chosen to obtain both matching and phase-correct feeding for a circular polarization at 250 GHz.

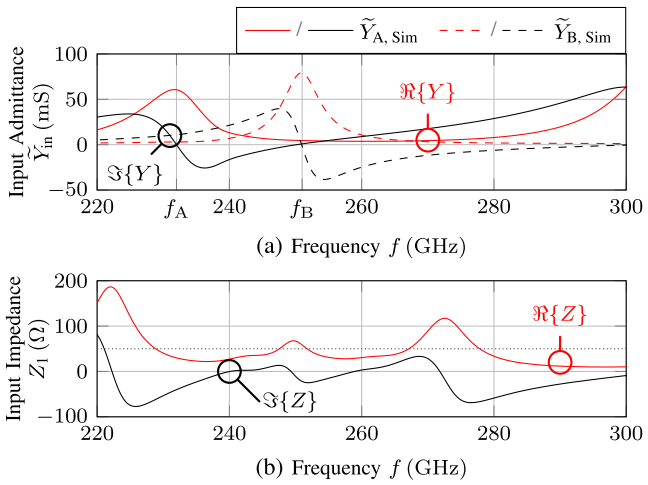

Fig. 6. Input admittance and impedance at different reference planes in the feeding network (see Fig. 5). (a) Input admittances of both antennas A and B, which are connected in parallel, yielding a frequency selectivity toward the larger admittance. (b) Total input impedance corresponding to a differential feeding of the antenna.

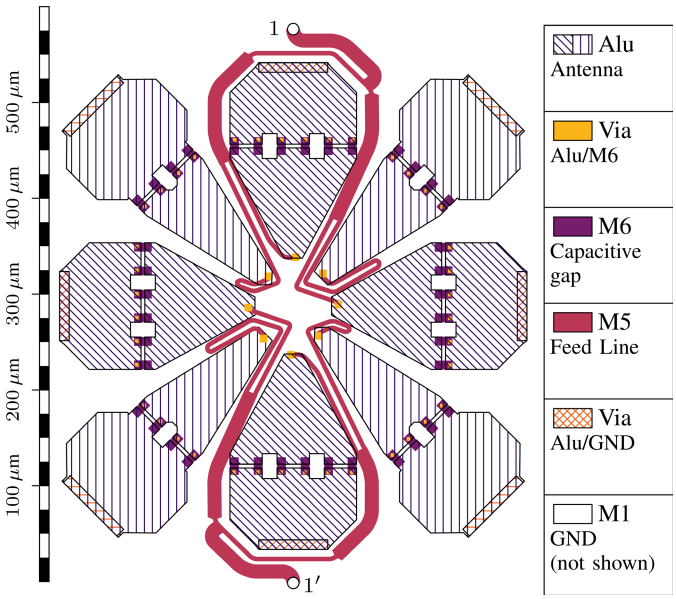

Fig. 7. Layout of the total antenna assembly including the circular arrangement of each four dipole arms A and B and the corresponding transmission-line-based feeding network realized on a separate metal layer. The feeding poles 1 and 1′ for connection to on-chip sources or a balun are highlighted as well.

and result in a phase shift to ideally radiate circularly polarized waves. A schematic of the desired feeding network topology is depicted in Fig. 5. At the center frequency of 250 GHz, the aforementioned antenna elements A and B should be fed with a phase according to their geometrical position to obtain a circular polarization, which will unavoidably result in a suboptimal operation at other frequencies. Starting at poles 1 and 1′, the antenna is designed for a differential feeding or a corresponding differential receiver. From each pole, two branches of ≈320 μm length are separated by a $\lambda/4$ transformer enabling both a balancing of the power per branch and a 90° phase shift necessary for the CP generation. Each branch then splits into two transmission lines of 90° and 135° electrical length, resulting in both a phase-correct feeding and the desired frequency selectivity for the antenna elements A and B.

Fig. 6 shows the input admittance and impedance levels at the different reference points given in Fig. 5. As it can be seen by comparing Figs. 3(a) and (b) and 6(a), the frequency selectivity results from the impedance transformation, where the high impedance of the antenna at resonance is transformed into a high admittance, which then accepts most of the power when connected in parallel ($\widetilde{Y}_A + \widetilde{Y}_B$). The total input impedance Z_1 can be finally matched by choosing a suitable characteristic impedance of the quarter-wavelength transformer at the poles 1 and 1′ [see Fig. 6(b)]. It should be emphasized that this feeding network enables a relatively wide matching bandwidth on the cost of a suboptimal CP generation at frequencies other than 250 GHz.

III. Antenna Assembly On-Chip

Fig. 7 shows the final layout of the circularly arranged antenna elements and the corresponding feeding network. To reduce the coupling to the antenna elements, the feeding network is located on a separate metal layer and connected by vias to the individual feeding points. For the characterization of the fabricated antenna, both poles 1 and 1′ are connected to a balun and a single-ended GSG-probing pad. The balun

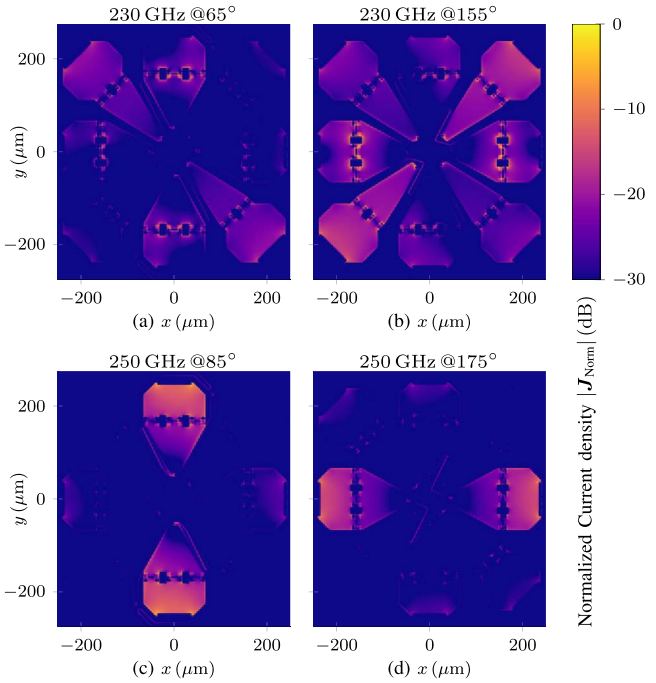

Fig. 8. Instantaneous electric current density in the top metal layers of the antenna at each two different time instances at (a) and (b) 230 GHz and (c) and (d) 250 GHz simulated with Empire XPU. The time instances (corresponding to 65°/155° and 85°/175°) are separated by 90° and chosen to indicate the peaking current density dipole, indicating the CP operation.

is furthermore fabricated in a back-to-back structure with identical line length, which allows measuring the balun and probing-pad losses.

The surface current density along the antenna is simulated using the full-wave FDTD solver Empire XPU and evaluated at 230 and 250 GHz. Fig. 8 shows the instantaneous current densities on the different metal layers projected into one plane with a dynamic range of 30 dB. The normalization is carried out globally for all phase angles, enabling a comparison of feeding amplitudes between different time instances. To indicate the phase-correct feeding, the field is evaluated at two time instances corresponding to a 90° phase delay. Whereas the feeding of the dipole arms is well separated and comparable in amplitude for 250 GHz, at 230 GHz, the unintended feeding of the vertical and horizontal dipole arms [see Fig. 8(b)] and an amplitude difference of ≈ 3 dB between the different time instances can be clearly seen, presumably resulting in a more elliptical polarization. This is a direct consequence of the feeding network design, which is optimally matched and phase-correctly fed at 250 GHz due to the $\lambda/4$ transformers. At the edges of the operation bandwidth, not only the matching but also the feeding phase are only suboptimal due to the decreased electrical length of the feeding lines (see Fig. 5), and as a consequence, the axial ratio degrades.

IV. CP Characterization at mm-Waves

For the antenna radiation pattern measurement, a spherical wafer antenna measurement system [24] is used. To minimize

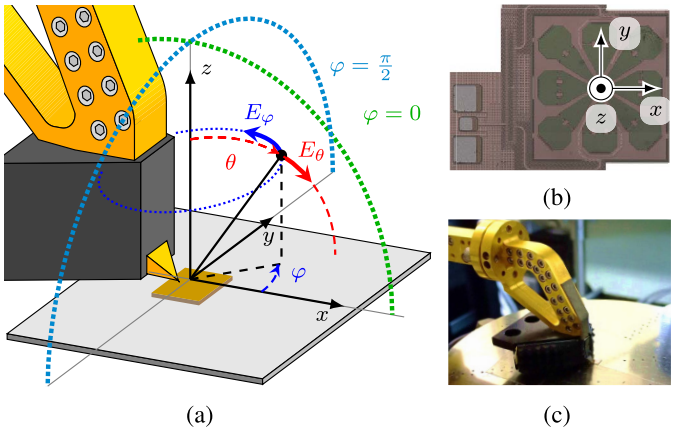

Fig. 9. (a) Drawing of the probe with the coordinate system used, (b) micrograph of the chip antenna with the coordinate system, and (c) photograph of the real probe contacting the chip antenna.

the chip area overhead, the probing pads are located close to the antenna. Consequently, the on-wafer probe is covered with thin-layer graphite absorbers to suppress reflections. Furthermore, only a part of the radiation pattern can be observed due to the shadowing of the probe [25], [26]. The cut planes and the coordinate system utilized for antenna characterization are depicted in Fig. 9(a).

To characterize the polarization, namely differentiate between LHCP and RHCP, phase-correct measurements of φ- and θ-polarization are used to calculate the RHCP and LHCP components according to [27, pp. 150], where the additional $(2)^{1/2}$ maintains the norm

$$E_{\mathrm{RHCP}} = \frac{E_\theta - \mathrm{j}E_\varphi}{\sqrt{2}}$$
$$E_{\mathrm{LHCP}} = \frac{E_\theta + \mathrm{j}E_\varphi}{\sqrt{2}}. \quad (1)$$

The phase-correct measurement of mm-waves is a difficult task, and consequently, different methods to characterize the purity of a CP have been presented and discussed in the literature. If a receiving linear polarized antenna is used, the gradual rotation of this antenna can be used to accurately measure the elliptical polarization either by many sampling points [28] or by estimating the ellipse based on few samples [25], reducing the necessity of phase-correct measurements. However, at least four gain-correct measurements need to be carried out compared with two gain- and phase-correct measurements, presumably doubling the necessary measurement time. Alternatively, different reflectors can be used for a time-gated characterization of the input reflection coefficient of the antenna [29], which can ultimately be used to characterize LHCP and RHCP, but the reflectors need to be relatively large to overcome the two-way path loss ($\propto r^{-4}$), rendering this method less suitable for radiation pattern measurement. Furthermore, CP reference antennas, which inherently receive LHCP or RHCP and thus do not require a phase-correct measurement of field components, could be used. Here, the typical waveguide-based solutions only provide a band-limited acceptable axial ratio [30], [31], reducing the applicability

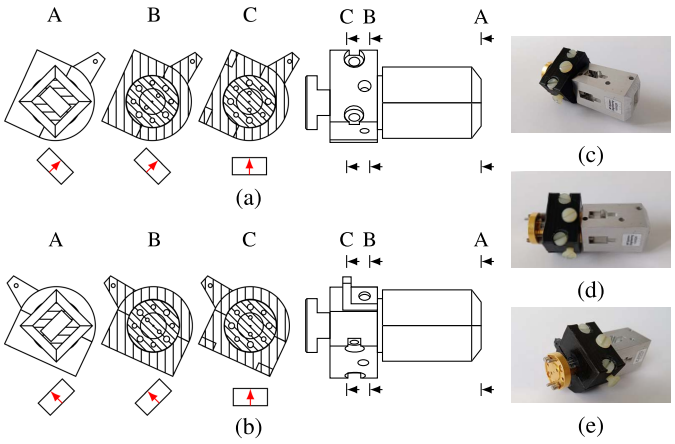

Fig. 10. Drawing of the rotating collet with different cross sections (a) in θ-polarization and (b) in φ-polarization and the photographs of the θ-polarized collet in (c) front-, (d) side-, and (e) back-view. The cross sections show (A) the horn aperture, (B) the rotating waveguide inside the collet, and (C) the fixed waveguide attached to the receiver. The boxes with red arrows indicate the waveguide orientation for each case.

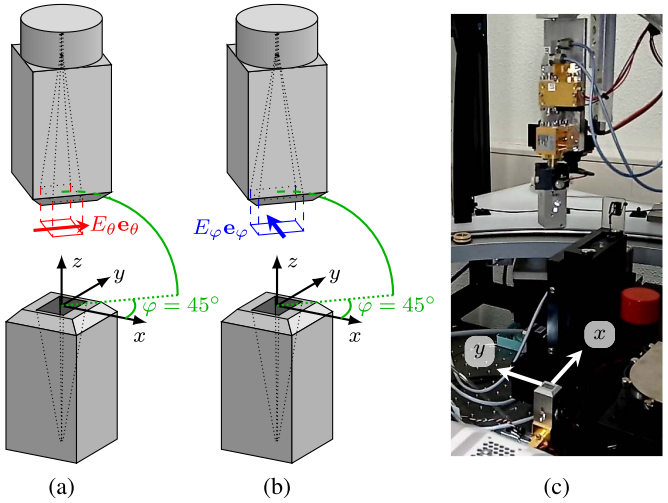

Fig. 11. Free-space measurement for characterization of the rotating collet with drawings for (a) θ-polarization rotated by 45°, (b) φ-polarization rotated by 45°, and (c) measurement of the rotated φ-polarization.

to narrow-band characterizations. Finally, simply rotating the receiving waveguide antenna seems a very practical and suitable solution, although it needs to be assured that no phase errors due to displacement [32] or cable bend [33] occur. This also rules out the use of a simple waveguide twist [34] for phase-correct measurements, since the mechanical process of reconnecting the flanges might introduce a receiver displacement in the order of the wavelength. Although the measurement setup utilized has been shown to characterize the radiation pattern with good phase stability, the effects of cable bends and temperature drift should be counteracted by the measurement procedure. Here, the receiving antenna is rotated at each measurement position to measure both polarizations in close succession, without any cable movement and only a neglectable temperature drift. A rotary joint would ideally fit this purpose if it were sufficiently phase-stable while rotated and manufacturable for the WR03 band [35]. Since a geometrical rotation of the receiving antenna by 90° would be sufficient, two rectangular waveguide flanges are rotated around their longitudinal axis by ±45°. The approach used here is similar to the approach in [36] except for the iris between the waveguide sections, which drastically increases the mechanical fabrication effort to improve input matching. Since the azimuthal misalignment of the waveguides is similar for both measurements, e.g., +45° for θ polarization and −45° for φ polarization, both amplitude and phase of the transmission characteristic should be highly comparable in the first place. To ensure the radial alignment during the rotation and axial alignment of the flanges, a cylindrical polylactide (PLA) collet is used. Fig. 10(a) and (b) shows technical drawings of the collet including the cross-sectional cuts highlighting the waveguide orientation, and Fig. 10(c)–(e) shows the photographs of the assembled horn in the rotating collet. The transmission parameter S_{21} and the corresponding uncertainty in phase and amplitude resulting from this fixture can be evaluated by measuring a well-known polarization for a number of repetitions. As in the CP measurement later, the measurement data of the single repetitions will be only compared with the data acquired in the next and former measurement to reduce temperature drift. As a reference, a horn antenna polarized in the x-direction (see Fig. 11) will be characterized with the measurement system setup to $\varphi = 45°$ and $\theta = 0°$, enabling a highly symmetrical characterization when measuring φ- and θ-polarization. Due to the symmetry, the measured transmission parameters should include the same free-space path loss, a polarization loss due to the misalignment of 45° for both the cases, and the actual loss of the transition. Accordingly, also the phase measured for both polarizations should be comparable (since mechanical differences could only occur due to axial misalignment of the rotation stage or imperfections in the flanges) and, more important, reproducible with low uncertainty. Fig. 12 shows the measured phase and amplitude difference between φ- and θ-polarization for 70 measurements. Comparing the transmission parameters for subsequent θ and ϕ measurements, the standard deviation of the resulting phase difference can be calculated and amounts to a maximum $\sigma_{\max} = 5.9°$ and a mean $\sigma_{\text{mean}} = 2.2°$, indicating a high phase-stability associated with the rotation of the receiving antenna. Concluding this section, the presented approach of using a misaligned waveguide to measure two orthogonal polarizations with high phase and amplitude repeatability works well, even for the very high frequencies utilized here.

V. mm-Wave Antenna Measurement

The characterization of the on-chip antenna by RHCP and LHCP is based on (1), where the θ and ϕ components at each measurement point are obtained utilizing the rotating waveguide from Section IV. The gain of the antenna under test (AUT) is accessed by comparing the transmission parameter S_{21} with a well-known horn antenna and additionally compensating for the losses of the mm-wave probe, as in [37],

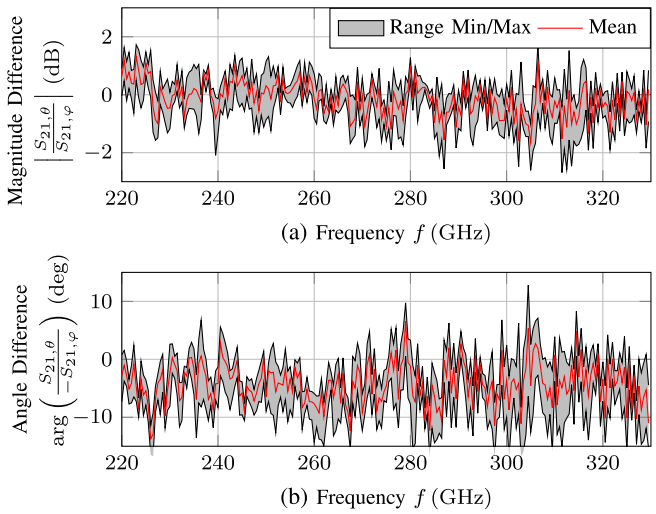

Fig. 12. (a) Magnitude difference and (b) phase difference between successive measurements of θ- and φ-polarization according to Fig. 11. For a total number of 70 measurements, the minimal, maximal, and averaged differences between the two polarizations are shown.

and the balun, according to

$$G_{\mathrm{AUT}} = \frac{1}{\left|S_{21,\mathrm{Balun}}\right|^2 \left|S_{21,\mathrm{Probe}}\right|^2} \frac{\left|S_{21,\mathrm{AUT}}\right|^2}{\left|S_{21,\mathrm{Horn}}\right|^2} G_{\mathrm{Horn}}. \tag{2}$$

The probe losses can be accessed by determination of the error terms of the mm-wave probe using on-wafer calibration standards (open, short, and load), and the losses of the balun on-chip are accessed by measuring the balun in a back-to-back configuration. The manufactured balun and the losses and phase associated with both baluns back-to-back are depicted in Fig. 13. Here, the balun itself is based on a rat-race coupler in the microstrip technique and uses an on-chip poly resistance for decoupling of the balanced ports. Furthermore, the input reflection coefficient and impedance of the antenna with the balun at the pads can be measured and compared with simulation results, as shown in Fig. 14. The pads consist of two ground pads connected to the on-chip ground (M1) and to the signal pad via a resonant loop to improve the transition from the CPW mode of the probe to the on-chip microstrip line. The corresponding full-wave simulations are carried out with the FDTD solver Empire XPU. Here, the agreement between simulation and measurement is acceptable, since especially the imaginary part of the input impedance is measured to be more inductive. It should be noted that this measurement cannot access the input impedance of the antenna at the feeding points 1 and 1′ (see Fig. 7), since a back-to-back measurement does not replace a full calibration. However, if antenna and balun are well matched, the losses within a single balun should be comparable, regardless of it being connected to the antenna or another balun.

For the characterization of the radiation pattern, the receiver is rotated around the AUT on a spherical coordinate system according to Fig. 9(a). Here, two cut planes are measured, and the $\varphi = 0°$-cut only covers a range of $0° \leq \theta \leq 90°$, since smaller angles usually suffer from the shadowing of the probe. Furthermore, the $\varphi = 90°$-cut is limited by $-90° \leq \theta \leq 50°$ to hinder a collision with the microscope [24].

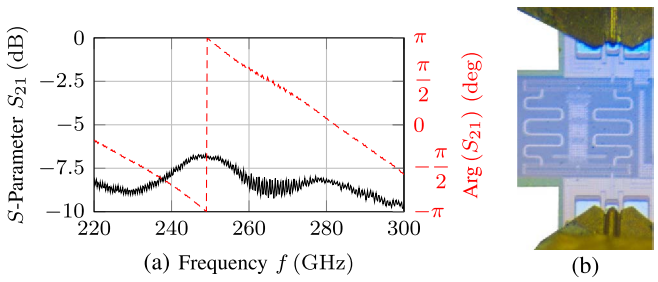

Fig. 13. Balun measurement (a) with the transmission parameter for both baluns in back-to-back configuration and (b) both probes contacting the pads.

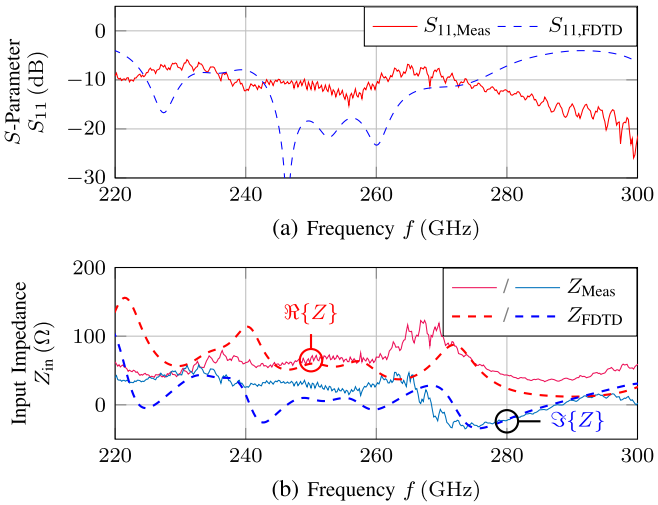

Fig. 14. Antenna measurement and simulation with (a) reflection coefficient S_{11} with the probe pads and balun and (b) input impedance at the probe pads.

Since the orthogonal components E_φ and E_θ of each measurement position are measured in direct subsequence, long-term phase drift due to temperature variations does not affect the accuracy of the measurement. This is indicated by the very good agreement of measured and simulated RHCP gain, depicted in Fig. 15(a) and (b), where only small undulations of the measurement indicate multipath contributions from reflections inside the measurement domain, most probably at the mm-wave probe [26], [37]. To avoid these contributions, the largest parts of the probe are covered with thin mm-wave absorbers, but the very sensitive probe tips and the metal parts nearby cannot be covered. The cut planes of the LHCP [see Fig. 15(c) and (d)] indicate large deviations between measured and simulated gains. It is supposed that the uncovered part of the probe, which is very close to or even in the near-field of the antenna, might convert parts of the RHCP into LHCP by reflection. This contributes to the measured LH component and might even exceed the LH component radiated by the antenna itself, which is supposedly the reason for the large deviation. Due to the very small distance between antenna and probe tip, the LHCP radiation from the antenna and LHCP radiation reflected by the probe cannot be separated by time-gating. To show that the large undesired LHCP is caused by the probe tip, the probe tip and a part of the absorber covering it have been modeled in EMPIRE XPU. The modeling is based on the micrographs of the probe tip at different focal planes in

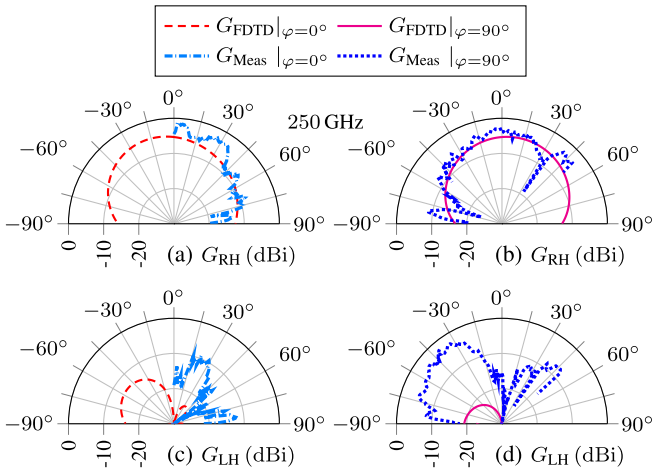

Fig. 15. Chip antenna measurement and simulation comparing the realized gain in two cut planes for (a) and (b) RHCP and (c) and (d) LHCP at 250 GHz.

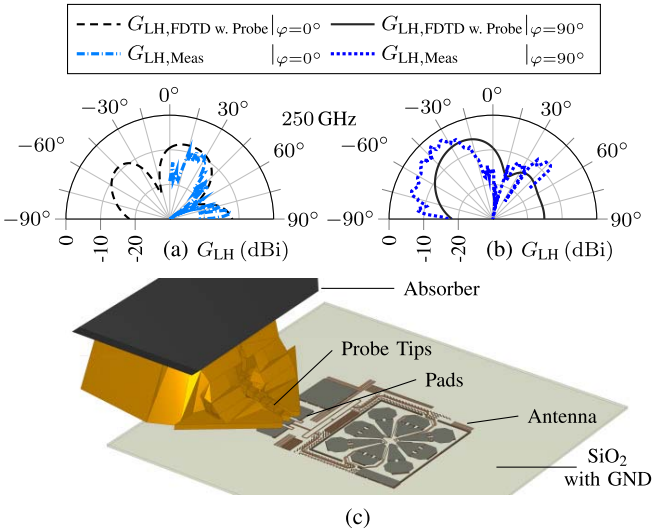

Fig. 16. (a) and (b) Chip antenna measurement and simulation with a probe model comparing the realized gain in two cut planes for LHCP at 250 GHz, and (c) screenshot from the simulation tool (EMPIRE XPU).

front and top views, and the results of the FDTD simulation for the LHCP gain at 250 GHz are shown in Fig. 16. Here, good agreement, especially considering the complex probe model [see Fig. 16(c)], between simulation and measurement is achieved, which confirms that the larger LHCP component of the measurement is an artifact of the probe.

Finally, the realized gain in the broadside direction over the frequency indicates a very good agreement between simulated and measured RHCP and LHCP, although a small frequency shift of $\approx$ 5 GHz is observable for both polarizations [see Fig. 17(a)]. The suppression of the LHCP far below 250 GHz will not be sufficient for most mobile systems, since the resulting polarization is strongly elliptical and thus dependent on the antenna orientation, and thus Tx and Rx antennas require an identical orientation on the final frontend. This can also be recognized by the axial ratio [see Fig. 17(b)], which indicates a dominant elliptical polarization.

Finally, the antenna aperture can be increased to increase the overall gain in the broadside direction, e.g., by a dielectric

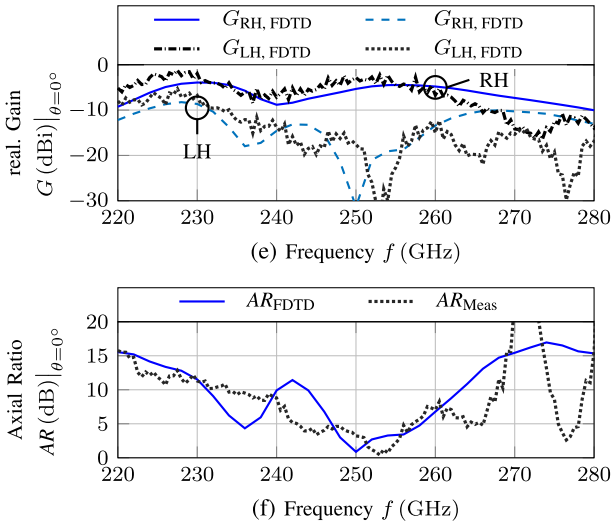

Fig. 17. Chip antenna measurement and simulation comparing (a) realized gain and (b) axial ratio over the frequency.

Fig. 18. (a) Micrograph of the antenna with positioned PTFE lens and (b) photograph of the contacted probe beneath the PTFE lens.

lens. The lens utilized here is a hyper-hemispherical lens of 800 μm height and 1000 μm diameter of polytetrafluorethylene (PTFE). Due to the low permittivity of PTFE and the utilized series capacitances in the antenna, only a low frequency-downshift and practically no deviation from the desired operation are expected. Theoretically, larger lenses would enable a larger aperture and a proportionally larger gain, but the probing pads need to remain accessible for the probe tips, limiting the maximum useable lens size. A micrograph of the PTFE lens on-chip and a photograph of the probe with the lens are depicted in Fig. 18. The measured realized gain with lens is depicted in Fig. 19, again in a very good agreement for the dominant RHCP over frequency, and again with unexpected large contributions of the undesired LHCP. It should be noted that the lens can only improve both RHCP and LHCP, and thus, the axial ratio cannot be improved by this measure. Over the whole frequency band between 220 and 260 GHz, the realized RHCP gain is extraordinarily constant given the resonant structure the antenna is based on. Again, the suppression of the LHCP is very weak at the edges of the frequency band in both simulation and measurement, which has already been explained by the feeding network designed for optimal CP operation at 250 GHz.

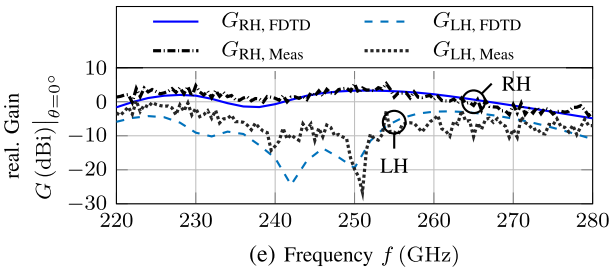

Fig. 19. Chip antenna with 1 mm PTFE lens comparing the realized gain in broadside direction over the frequency.

VI. Conclusion

This article demonstrates a design approach for achieving an increased operation bandwidth for on-chip antennas. The main concept combines a feeding and matching network, which ensures frequency selectivity toward the suitable antenna and maintains a circular polarization at the design frequency. The feeding network operates suboptimally with increasing difference between operation and design frequency, resulting mainly in elliptically polarized radiation. Furthermore, the dipole arms fed by the feeding network are geometrically tailored for their application, maximizing the utilization of the available chip area. By introducing a simple rotating collet for changing the polarization of the receiving horn, the CP radiation pattern has been measured and compared with simulation with excellent agreement. For the desired radar application, this antenna needs to be mirrored to achieve a complementary LHCP antenna, which could be used with the presented antenna as a Tx and Rx antenna pair. Since the operation bandwidth of the antenna is strongly limited by the realized elliptical polarization, and not by the antenna mismatch, the feeding network could be optimized toward fulfilling the ideal CP phase shift at the operation frequencies of the individual dipoles, instead of the center frequency, on the cost of the matching and frequency selectivity. Only then, the antennas could be arbitrarily oriented within a Tx–Rx system without significant signal loss.

Acknowledgment

The authors are grateful to Infineon Technologies for manufacturing and providing the test chip with the on-chip antenna and to Klaus Aufinger, Infineon Technologies, for his extensive and valuable consultation.

References

[1] K. B. Cooper *et al.*, "Penetrating 3-D imaging at 4- and 25-m range using a submillimeter-wave radar," *IEEE Trans. Microw. Theory Techn.*, vol. 56, no. 12, pp. 2771–2778, Dec. 2008.

[2] D. M. Mittleman, "Frontiers in terahertz sources and plasmonics," *Nature Photon.*, vol. 7, no. 9, pp. 666–669, Sep. 2013.

[3] M. Caris, S. Stanko, S. Palm, R. Sommer, A. Wahlen, and N. Pohl, "300 GHz radar for high resolution SAR and ISAR applications," in *Proc. 16th Int. Radar Symp. (IRS)*, Dresden, Germany, Jun. 2015, pp. 577–580.

[4] C. Waldschmidt, J. Hasch, and W. Menzel, "Automotive radar—From first efforts to future systems," *IEEE J. Microw.*, vol. 1, no. 1, pp. 135–148, Jan. 2021.

[5] A. Shamim, K. N. Salama, E. A. Soliman, and S. Sedky, "On-chip antenna: Practical design and characterization considerations," in *Proc. 14th Int. Symp. Antenna Technol. Appl. Electromagn. Amer. Electromagn. Conf.*, Ottawa, ON, Canada, Jul. 2010, pp. 1–4.

[6] A. Fischer, Z. Tong, A. Hamidipour, L. Maurer, and A. Stelzer, "77-GHz multi-channel radar transceiver with antenna in package," *IEEE Trans. Antennas Propag.*, vol. 62, no. 3, pp. 1386–1394, Mar. 2014.

[7] V.-S. Trinh, H. N. Chen, and J.-D. Park, "A +3-dBm-EIRP 240-GHz circular-polarized radiator utilizing a sub-THz PA in 65-nm CMOS," *IEEE Microw. Wireless Compon. Lett.*, vol. 30, no. 4, pp. 399–402, Apr. 2020.

[8] K. Statnikov, N. Sarmah, J. Grzyb, S. Malz, B. Heinemann, and U. R. Pfeiffer, "A 240 GHz circular polarized FMCW radar based on a SiGe transceiver with a lens-integrated on-chip antenna," in *Proc. 44th Eur. Microw. Conf.*, Rome, Italy, Oct. 2014, pp. 1750–1753.

[9] S. M. Bowers, A. Safaripour, and A. Hajimiri, "An integrated slot-ring traveling-wave radiator," *IEEE Trans. Microw. Theory Techn.*, vol. 63, no. 4, pp. 1154–1162, Apr. 2015.

[10] Z. Chen, C.-C. Wang, H.-C. Yao, and P. Heydari, "A BiCMOS W-band 2×2 focal-plane array with on-chip antenna," *IEEE J. Solid-State Circuits*, vol. 47, no. 10, pp. 2355–2371, Oct. 2012.

[11] X.-Y. Bao, Y.-X. Guo, and Y.-Z. Xiong, "60-GHz AMC-based circularly polarized on-chip antenna using standard 0.18-μm CMOS technology," *IEEE Trans. Antennas Propag.*, vol. 60, no. 5, pp. 2234–2241, May 2012.

[12] X. Bai, S. Qu, and K. B. Ng, "Millimeter-wave cavity-backed patch-slot dipole for circularly polarized radiation," *IEEE Antennas Wireless Propag. Lett.*, vol. 12, pp. 1355–1358, 2013.

[13] A. B. Guntupalli and K. Wu, "60-GHz circularly polarized antenna array made in low-cost fabrication process," *IEEE Antennas Wireless Propag. Lett.*, vol. 13, pp. 864–867, 2014.

[14] S. Ghosh and D. Sen, "An inclusive survey on array antenna design for millimeter-wave communications," *IEEE Access*, vol. 7, pp. 83137–83161, 2019.

[15] B. Sievert, D. Erni, and A. Rennings, "Resonant antenna periodically loaded with series capacitances for enhanced radiation efficiency," in *Proc. 12th German Microw. Conf. (GeMiC)*, Stuttgart, Germany, Mar. 2019, pp. 20–23.

[16] B. Sievert, J. T. Svejda, J. Wittemeier, N. Pohl, D. Erni, and A. Rennings, "Equivalent circuit model separating dissipative and radiative losses for the systematic design of efficient microstrip-based on-chip antennas," *IEEE Trans. Microw. Theory Techn.*, vol. 69, no. 2, pp. 1282–1294, Feb. 2021.

[17] R. E. Munson, "Microstrip antennas," in *Antenna Engineering Handbook*, R. C. Johnson, Ed., 3rd ed. New York, NY, USA: McGraw-Hill, 1993.

[18] L. Lewin, "Radiation from discontinuities in strip-line," *Proc. IEE C, Monographs*, vol. 107, no. 12, pp. 163–170, Sep. 1960.

[19] L. Lewin, "Spurious radiation from microstrip," *Proc. Inst. Elect. Eng.*, vol. 125, no. 7, pp. 633–642, Jul. 1978.

[20] H. Sobal, "Radiation conductance of open-circuit microstrip (correspondence)," *IEEE Trans. Microw. Theory Techn.*, vol. MTT-19, no. 11, pp. 885–887, Nov. 1971.

[21] D. B. Brick, "The radiation of a Hertzian dipole over a coated conductor," Cruft Lab., Harvard Univ., Cambridge, MA, USA, Tech. Rep. 172, May 1953.

[22] R. Owens, "Accurate analytical determination of quasi-static microstrip line parameters," *Radio Electr. Eng.*, vol. 46, no. 7, pp. 360–364, Jul. 1976.

[23] H. Wheeler, "Transmission-line properties of a strip on a dielectric sheet on a plane," *IEEE Trans. Microw. Theory Techn.*, vol. MTT-25, no. 8, pp. 631–647, Aug. 1977.

[24] B. Sievert, J. T. Svejda, D. Erni, and A. Rennings, "Spherical mm-wave/THz antenna measurement system," *IEEE Access*, vol. 8, pp. 89680–89691, 2020.

[25] D. Titz, F. Ferrero, and C. Luxey, "Development of a millimeter-wave measurement setup and dedicated techniques to characterize the matching and radiation performance of probe-fed antennas," *IEEE Antennas Propag. Mag.*, vol. 54, no. 4, pp. 188–203, Aug. 2012.

[26] L. Boehm, M. Hitzler, F. Roos, and C. Waldschmidt, "Probe influence on integrated antenna measurements at frequencies above 100 GHz," in *Proc. 46th Eur. Microw. Conf.*, London, U.K., Oct. 2016, pp. 552–555.

[27] C. A. Balanis, *Advanced Engineering Electromagnetics*, 2nd ed. Hoboken, NJ, USA: Wiley, 2012.

[28] B. Goettel, J. Schaefer, H. Gulan, W. Winkler, and T. Zwick, "Double circularly polarized on-chip antenna for a 120–130 GHz amplitude monopulse radar," in *Proc. Eur. Radar Conf. (EURAD)*, London, U.K., Oct. 2016, pp. 409–412.
[29] S. Bhardwaj, N. K. Nahar, and J. L. Volakis, "Novel phaseless gain characterization for circularly polarized antennas at mm-wave and THz frequencies," *IEEE Trans. Antennas Propag.*, vol. 63, no. 10, pp. 4263–4270, Oct. 2015.
[30] S. Bhardwaj and J. L. Volakis, "Hexagonal waveguide based circularly polarized horn antennas for sub-mm-wave/terahertz band," *IEEE Trans. Antennas Propag.*, vol. 66, no. 7, pp. 3366–3374, Jul. 2018.
[31] C. Shu *et al.*, "A wideband dual-circular-polarization horn antenna for mmWave wireless communications," *IEEE Antennas Wireless Propag. Lett.*, vol. 18, no. 9, pp. 1726–1730, Sep. 2019.
[32] J. G. Marin and J. Hesselbarth, "Circularly-polarized on-chip dielectric resonator antenna," in *Proc. 12th Eur. Conf. Antennas Propag. (EUCAP)*, London, U.K., Apr. 2018, pp. 1–4.
[33] M. Hitzler, S. Bader, and C. Waldschmidt, "Key aspects of robot based antenna measurements at millimeter wave frequencies," in *Proc. 8th Eur. Conf. Antennas Propag.*, The Hague, The Netherlands, Apr. 2014, pp. 392–396.
[34] T. Zwick, C. Baks, U. Pfeiffer, D. Liu, and B. Gaucher, "Probe based MMW antenna measurement setup," in *Proc. IEEE Antennas Propag. Soc. Symp.*, vol. 1, Jun. 2004, pp. 747–750.
[35] M. Marschner, F. Baum, and W. Keusgen, "Design of a WR10 rotary joint with two 3D-printed TE_{01} mode transducers," in *Proc. 94th Microw. Meas. Symp. (ARFTG)*, San Antonio, TX, USA, Jan. 2020, pp. 1–4.
[36] M. D. Blech, S. Koch, and S. Saito, "Rectangular waveguide based polarizer for mm-wave antenna measurements," in *Proc. 6th Eur. Conf. Antennas Propag. (EUCAP)*, Mar. 2012, pp. 3487–3490.
[37] S. Beer and T. Zwick, "Probe based radiation pattern measurements for highly integrated millimeter-wave antennas," in *Proc. 4th Eur. Conf. Antennas Propag.*, Barcelona, Spain, Apr. 2010, pp. 1–5.

Benedikt Sievert (Member, IEEE) was born in Krefeld, Germany. He received the B.Sc. and M.Sc. degrees in electrical engineering/high-frequency systems from the University of Duisburg-Essen, Duisburg, Germany, in 2017 and 2019, respectively.

Since 2017, he has been a member of the Laboratory of General and Theoretical Electrical Engineering, University of Duisburg-Essen. His research interests include mm-wave on-chip antennas, electromagnetic metamaterials, and theoretical and computational electromagnetics.

Jonathan Wittemeier was born in Lünen, Germany. He received the B.Sc. and M.Sc. degrees in electrical engineering and information technology from the TU Dortmund University, Dortmund, Germany, in 2014 and 2016, respectively.

From 2016 to 2017, he worked in the automotive industry as a Software Developer. Since 2017, he has been a Research Assistant with the Institute of Integrated Systems, Ruhr University Bochum, Bochum, Germany. His current research interests include mm-wave radar, MMIC design using silicon–germanium, and MIMO algorithms.

Jan Taro Svejda (Member, IEEE) received the B.Sc. degree in electrical engineering from the University of Applied Science, Düsseldorf, Germany, in 2008, and the M.Sc. degree in electrical engineering and information technology and the Dr.-Ing. degree in X-nuclei based magnetic resonance imaging from the University of Duisburg-Essen, Duisburg, Germany, in 2013 and 2019, respectively.

He is currently a Research Assistant with the Department of General and Theoretical Electrical Engineering, University of Duisburg-Essen, where he is involved in teaching several lectures and courses mainly in the field of electrical engineering. His general research interest includes all aspects of theoretical and applied electromagnetics, currently focusing on medical applications, electromagnetic metamaterials, and scientific computing methods.

Nils Pohl (Senior Member, IEEE) received the Dipl.-Ing. and Dr.-Ing. degrees in electrical engineering from Ruhr University Bochum, Bochum, Germany, in 2005 and 2010, respectively.

From 2006 to 2011, he was a Research Assistant with Ruhr University Bochum, where he was involved in integrated circuits for millimeter-wave (mm-wave) radar applications and became an Assistant Professor in 2011. In 2013, he became the Head of the Department of mm-wave Radar and High Frequency Sensors, Fraunhofer Institute for High Frequency Physics and Radar Techniques, Wachtberg, Germany. In 2016, he became a Full Professor for Integrated Systems with Ruhr University Bochum. He has authored or coauthored more than 100 scientific articles and has issued several patents. His current research interests include ultrawideband mm-wave radar, design and optimization of mm-wave integrated SiGe circuits and system concepts with frequencies up to 300 GHz and above, and frequency synthesis and antennas.

Dr. Pohl is a member of Verband der Elektrotechnik Elektronik Informationstechnik e.V. (VDE), Informationstechnische Gesellschaft (ITG), European Microwave Association (EUMA), and Union Radio-Scientifique Internationale (URSI). He was a corecipient of the 2009 EEEfCom Innovation Award, the 2012 EuMIC Prize, and the 2015 Best Demo Award of the IEEE Radio Wireless Week, and a recipient of the Karl-Arnold Award of the North Rhine-Westphalian Academy of Sciences, Humanities and the Arts in 2013 and the IEEE MTT Outstanding Young Engineer Award in 2018.

Daniel Erni (Member, IEEE) received the Diploma degrees in electrical engineering from the University of Applied Sciences in Rapperswil (OST), Rapperswil-Jona, Switzerland, and ETH Zürich, Zürich, Switzerland, in 1986 and 1990, respectively, and the Ph.D. degree in laser physics from the Laboratory for Electromagnetic Fields and Microwave Electronics, ETH Zürich, in 1996.

Since 1990, he has been with the Laboratory for Electromagnetic Fields and Microwave Electronics, ETH Zürich, where he was the Founder and the Head of the Communication Photonics Group from 1995 to 2006. Since October 2006, he has also been a Full Professor with the Laboratory for General and Theoretical Electrical Engineering, University of Duisburg-Essen, Duisburg, Germany. He is a Co-Founder of the spin-off company airCode on flexible printed RFID technology Hamm, Germany. His current research interests include optical interconnects, nanophotonics, plasmonics, advanced solar cell concepts, optical and electromagnetic metamaterials, RF, mm-wave, and THz engineering, biomedical engineering, bioelectromagnetics, marine electromagnetics, computational electromagnetics, multiscale and multiphysics modeling, numerical structural optimization, and science and technology studies (STS).

Dr. Erni is a fellow of the Electromagnetics Academy, a member of the Center for Nanointegration Duisburg-Essen (CeNIDE), and a member of the Swiss Physical Society (SPS), the German Physical Society (DPG), and the OPTICA.

Andreas Rennings (Member, IEEE) studied electrical engineering at the University of Duisburg-Essen, Duisburg, Germany. He carried out his diploma work during a stay at the University of California at Los Angeles, Los Angeles, CA, USA. He received the Dipl.-Ing. and Dr.-Ing. degrees from the University of Duisburg-Essen in 2000 and 2008, respectively.

From 2006 to 2008, he was with IMST GmbH, Kamp-Lintfort, Germany, where he was an RF Engineer. Since then, he has been a Senior Scientist and a Principal Investigator at the Laboratory for General and Theoretical Electrical Engineering, University of Duisburg-Essen. His general research interest includes all aspects of theoretical and applied electromagnetics, currently with a focus on medical applications and on-chip millimeter-wave/THz antennas.

Dr. Rennings received several awards, including a Student Paper Price at the 2005 IEEE Antennas and Propagation Society International Symposium and the Verband der Elektrotechnik Elektronik Informationstechnik e.V. (VDE)-Promotionspreis 2009 for the dissertation.